Thermodynamic driving mechanisms for the formation of global precipitation extremes and ecohydrological effects

Jiabo YIN[1], Shenglian GUO[1*], Jun WANG[1], Jie CHEN[1], Quan ZHANG[1], Lei GU[2], Yan YANG[3], Jing TIAN[1], Lihua XIONG[1] & Yao ZHANG[4]

[1] State Key Laboratory of Water Resources and Hydropower Engineering Science, Wuhan University, Wuhan 430072, China;
[2] School of Civil and Hydraulic Engineering, Huazhong University of Science and Technology, Wuhan 430074, China;
[3] Key Laboratory of Surveying and Mapping Science and Geospatial Information Technology of MNR, Chinese Academy of Surveying and Mapping, Beijing 100830, China;
[4] College of Urban and Environmental Sciences, Peking University, Beijing 100871, China

Abstract Global warming has altered the thermodynamic and dynamic environments of climate systems, affecting the biogeochemical processes between the geosphere and atmosphere, which has significant impacts on precipitation extremes and the terrestrial carbon budget of ecosystems. Existing studies have reported a hook structure for precipitation extreme-temperature relationships but have rarely examined the underlying physical mechanisms. Previous studies have also failed to quantify the impact of precipitation on ecosystem productivity, hindering the assessment of future extreme climatic hazards and potential ecosystem risks. To reveal the thermodynamic driving mechanisms for the formation of global precipitation extremes and ecohydrological effects, this study utilizes over ten multisource datasets (i.e., satellite, reanalysis, climate model, land surface model, machine learning reconstruction, and flux tower measurements). We first assess the response of water-heat-carbon flux to precipitation extremes and explain the underlying physical mechanisms behind the hook structures in terms of atmospheric thermodynamics and dynamics. Based on outputs from five global climate models (GCMs) under ISIMIP3b, we project future changes in the hook structures as well as their impacts on precipitation extremes. Finally, we discuss the impact of precipitation on the terrestrial carbon budget by using outputs from the CLM4.5 model. The results show that precipitation extremes are usually accompanied by strong exchanges of water and heat and demonstrate a nonlinear relationship between precipitation and ecosystem productivity. The intensity (duration) of extreme precipitation is intensifying (decreasing) over most areas of the globe, whereas three-dimensional precipitation events are becoming more concentrated. Atmospheric dynamics play a key role in shaping the hook structure. The structure is not stable; it shifts under climate change and is projected to result in a 10–40% intensification in precipitation by the end of this century. Moderate levels of precipitation contribute to carbon assimilation in ecosystems, and the response of the carbon budget to precipitation is relatively stable under climate change.

Keywords Climate change, Precipitation extremes, Thermodynamics, Ecosystem, Carbon budget

1. Introduction

Since the second industrial revolution, humans have widely used fossil fuels, which has led to a sharp rise in greenhouse gas concentrations in the atmosphere, altering the energy budget balance and changing the biogeochemical cycle of the Earth's geosphere and atmosphere. As the spatiotemporal distribution of water resources is becoming more im-

* Corresponding author (email: slguo@whu.edu.cn)

balanced, hydrometeorological extremes (e.g., rainstorms and flooding) are occurring more frequently, posing a major challenge to the sustainable development of ecosystems and human society (Wing et al., 2022; Piao et al., 2022). Precipitation is an important process and a key element of the hydrological cycle, and the frequency and intensity of precipitation extremes have significantly intensified in most areas of the globe since the beginning of the 21st century. These changes have led to a series of water-related disasters, such as flash flooding, urban waterlogging and debris flows, with annual losses of over $30 billion globally (Roxy et al., 2017). For example, several large-scale and heavy rains occurred along the Yangtze River in 2020, resulting in a river-scale flood hazard and causing direct economic losses of nearly ¥70 billion. In July 2021, Zhengzhou in Henan Province was hit by a series of heavy rainstorms, which affected 14.814 million people and a large area of crops and caused direct economic losses of ¥133.715 billion. To cope with the above challenges, it is necessary to investigate the evolution mechanisms of precipitation extremes under climate change.

Precipitation extremes not only have major impacts on socioeconomic development but also pose lasting and irrecoverable damage to terrestrial ecosystems, which severely threatens national food security and ecological security. From 1979 to 2008, three major global grain yields showed large interannual variations; climate change accounted for 32–39% of these fluctuations, while precipitation was a decisive factor in grain yields through most regions of China, South Asia and the U.S. (Vogel et al., 2019). Precipitation affects ecosystems through physiological, chemical, physical and associated processes, such as by altering the growth environment of vegetation (including oxygen supply, light and temperature), thus affecting plant respiration and photosynthesis as well as changing their nutrient supply channels. In recent years, some attention has been directed at investigating the impacts of precipitation events on ecosystem productivity. For example, Zampieri et al. (2017) found a dynamic response relationship between precipitation, soil moisture and crop yield; heavy rain is prone to lead to nutrient loss and flooding stress in rice, thus resulting in crop yield reductions. Jian et al. (2021) found that short durations of heavy precipitation may cause physical damage to plants, and sustained cold temperatures and weak radiation during long durations of precipitation events can further increase the risk of crop yield reductions. Vegetation plays a key role in the earth's carbon cycle; plants assimilate carbon in the form of organic carbon through photosynthesis. As the largest flux in the earth's carbon cycle, a change in gross primary productivity (GPP) affects the entire carbon cycle, but the spatiotemporal dynamics of GPP are also affected by climate change. Green et al. (2020) found that the relationship between GPP and precipitation differed greatly under different

vegetation types and climatic conditions; precipitation and GPP were significantly and positively intercorrelated in the savanna region, while in the Amazon rainforest, increased precipitation weakened vegetation photosynthesis. Overall, the impacts of precipitation extremes on terrestrial ecosystem productivity and the carbon budget are still poorly understood.

With ongoing global changes and associated ecological research, a complicated feedback phenomenon in the land-vegetation-water–atmosphere system has been reported, which not only determines the energy and water balance in a basin or at a regional scale but also plays an important role in affecting the global climate system (Wen et al., 2019). Some studies have attempted to examine the evolution mechanisms of precipitation extremes from the perspective of atmospheric thermodynamics. According to the Clausius-Clapeyron (C-C) thermodynamic relationship, Allan and Soden (2008) found that the atmospheric water vapor holding capacity increases at a rate of approximately 6.8% $°C^{-1}$ (C-C scaling) with warming temperature. As water vapor in the troposphere (especially that in the boundary layer) is the material basis for precipitation generation, numerous studies have established governing equations for atmospheric water vapor content and examined the response of daily global precipitation extremes to climate warming. The results of these studies have shown that precipitation extremes in most regions of the globe show a sub-C-C scaling rate (less than 6.8% $°C^{-1}$) or a negative rate (Zeder and Fischer, 2020). A few studies have found that the response of precipitation extremes to climate change varies at different temporal scales, and the scaling rates of subdaily (e.g., hourly or minutely) precipitation extremes may exceed 6.8% $°C^{-1}$ (Lenderink and Van Meijgaard, 2008; Prein et al., 2017; Fowler et al., 2021). Recently, some studies have reported that precipitation extremes in most regions of the globe show a hook structure with near-surface temperatures, where extremes first increase and then decrease (Yin et al., 2018; Sullivan et al., 2020). The hook structure has prompted extensive discussions on the application of the C-C thermodynamic relationship. For example, Utsumi et al. (2011) and Gao et al. (2018) attributed the hook structure of daily precipitation extremes to a decline in precipitation duration at higher temperatures. Barbero et al. (2018) hold that relative humidity (RH) plays an important role in modulating precipitation extremes in Australia and that the dew point temperature can represent the water vapor condition better than air temperature. Wang et al. (2017) and Gao et al. (2020) found that a change in RH is a key driver for shaping the hook structure, and the cooling effects of precipitation and weather systems on temperature also play important roles. Roderick et al. (2019) further found that when the air temperature exceeded 28°C, the total column water vapor (TCWV) of tropical areas decreased with warming tem-

perature, thus resulting in precipitation declines. Overall, the occurrence and development of precipitation depend both on water vapor content and on the stability of atmospheric stratification, which involves complex atmospheric thermo-dynamic and dynamic effects, which are related to water and heat factors (such as humidity, vertical velocity and convective available potential energy (CAPE)). Previous studies have rarely investigated the comprehensive driving mechanisms for extreme precipitation evolution, and the thermodynamic and dynamic responses of these events as well as their ecohydrological effects are still poorly understood.

To reveal the thermodynamic driving mechanisms of global precipitation extremes and their ecohydrological effects, this study utilizes over ten multisource datasets (i.e., satellite, reanalysis, climate model, land surface model, machine learning reconstruction, and flux tower measurements). We first assess the response of water-heat-carbon flux to precipitation extremes and examine the impact of hydrometeorological variables (e.g., temperature, precipitation, soil moisture and terrestrial water storage) on an ecosystem carbon budget. We then investigate changes in the intensity and duration of both subdaily and daily precipitation extremes and examine the frequency, coverage area and average intensity of three-dimensional precipitation events. Based on extended Clausius-Clapeyron relationships, we identify the scaling structure of multitemporal precipitation extremes and their peak point temperature (T_{pp}). We attribute the hook structures to vapor and energy factors (i.e., RH, CAPE and TCWV) and attempt to explain the physical mechanisms of the hook structures. Using projections from five global climate models (GCMs) and three shared socio-economic pathways (SSPs) under ISIMIP3b, we project the shifts in the hook structures and their impacts on precipitation extremes. Finally, we investigate the impacts of precipitation on ecosystem carbon budgets by using outputs from the CLM4.5 model.

2. Data and materials

2.1 Multisatellite precipitation, GRACE and reanalysis

The MSWEP-V2 dataset is a second-generation global multisatellite quantitative precipitation product released by Princeton University, with spatiotemporal resolutions of 3 h and 0.1°. It integrates multiple satellite retrieval data (including CMORPH, GridSat, GSMaP and TRMM, etc.), over 70,000 ground stations (including WorldClim, GHCND, GSOD and GPCC) and reanalysis data (ERA-Interim and JRA-55) and has been corrected by global runoff observations (Beck et al., 2019). In this study, the 3 h precipitation data from the MSWEP-V2 dataset from 1979 to 2017 are used.

ERA5 is a fifth-generation atmospheric reanalysis dataset produced by the European Centre for Medium Range Weather Forecasts (ECMWF), which has provided hourly meteorological data with a spatial resolution of 0.25° globally since 1979 (Nogueira, 2020). In this study, we collect hourly precipitation, 2 m temperature, 2 m dew point temperature, air pressure, moisture flux convergence (MFC), latent heat flux, sensible heat flux, convection inhibition energy (CIN), CAPE and TCWV from 1979 to 2020. We also use hourly RH at the 1000 hPa level and finally integrate all the variables into a daily scale.

The GRACE/GRACE-FO satellite can effectively reflect the gravity changes caused by snow and ice, surface water, soil water, groundwater, and human factors, thus enabling the monitoring of the terrestrial water storage anomaly (TWSA) signal (Sun et al., 2015; Deng et al., 2022). The latest sixth generation (RL06) products generated by the Jet Propulsion Laboratory (JPL) of the California Institute of Technology in the U.S., the Center for Space Research (CSR) at the University of Texas at Austin, and NASA's Goddard Space Flight Center (GSFC) are used in this study. These products all provide monthly equivalent water height data based on the mass concentration block (mascon) solution. The three GRACE/GRACE-FO datasets are interpolated to a 0.5°×0.5° grid, and the global monthly TWSA series during 2002–2020 are finally obtained by averaging these products at each time step.

2.2 FLUXNET2015 dataset and climate model outputs

The FLUXNET2015 dataset contains observational records from 212 flux towers around the world, providing a new way to assess carbon-water-energy exchange processes between the biosphere and atmosphere. In this study, 69 flux stations with more than 5 observational years were screened, covering a variety of vegetation types, including grasslands, evergreen needleleaf forest, evergreen broadleaf forest, deciduous broadleaf forest and croplands (Figure 1). To investigate the processes for the water and carbon budget of ecosystems, we use several variables, such as 30 min (or hourly) precipitation, soil water content (including all soil layers), GPP and total ecosystem respiration (TER). TER contains both vegetation autotrophic respiration and soil heterotrophic respiration. These data are processed following a consistent and uniform processing pipeline. We use precipitation and soil moisture that are gap-filled using the marginal distribution method. NEP is obtained using a variable friction velocity (u^*) threshold for each year, with references selected on the basis of model efficiency, and is partitioned into GPP and TER following the night-time partitioning method. We also use a 4D solar-induced chlorophyll fluorescence (SIF) dataset with a spatial resolution of 0.5° covering 2000–2020, which is generated by training a machine learning algorithm on the daily OCO-2 SIF ob-
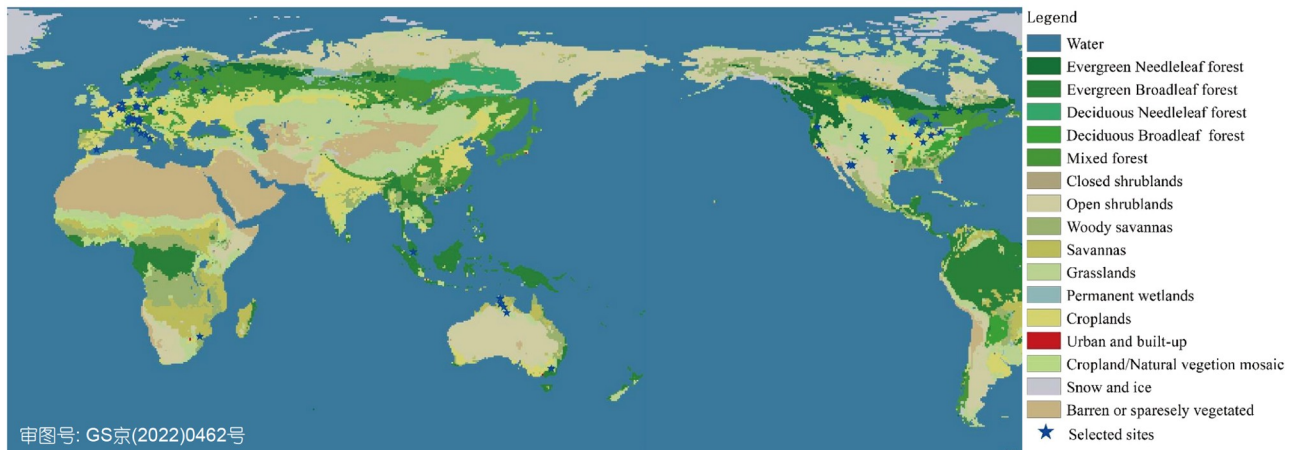
Figure 1   Global land use/cover types and 69 selected flux towers. Data source: MODIS MCD12Q1.

servations with colocation nadir BRDF-adjusted reflectance.

For the purpose of projecting future climatic conditions, the outputs of GCMs under the Coupled Model Intercomparison Project Phase 6 (CMIP6) are used. Compared with its predecessor (CMIP5), CMIP6 is constrained by a matrix framework of both SSP and the representative concentration pathway (RCP). As the GCM outputs have coarse spatial resolution and large systematic biases, Lange (2019) employed a parametric quantile mapping approach based on trend preservation to correct the biases of eleven daily variables (e.g., precipitation and temperature) and released these data under three SSPs (SSP126, 370, and 585) under ISIMIP3b. During the bias correction procedure, this dataset takes the interdependence of different variables into consideration and is produced at a uniform spatial resolution (0.5°×0.5°). The ISIMIP3b dataset includes outputs from five GCMs: GFDL-ESM4, IPSL-CM6A-LR, MPI-ESM1-2-HR, MRI-ESM2-0 and UKESm1-0-LL. In this study, the daily average temperature and total precipitation from three SSPs and five GCMs (15 scenarios) under the ISMIP3b are used, and the historical (future) period is set to 1985–2014 (2071–2100).

To simulate the response of ecosystem productivity to climate change, it is usually necessary to build coupled models of earth system models and land surface models. As ISIMIP3b has not released carbon flux data, the corrected outputs of GFDL-ESM2 M under the ISIMIP2b framework are used to drive the CLM4.5 model, and monthly carbon flux data under two RCPs (RCP2.6 and RCP6.0) from 1985 to 2099 are obtained. The CLM4.5 outputs contain GPP, autotrophic respiration and heterotrophic respiration, and the TER and NEP data are further calculated. CLM4.5 is the land surface module of the community earth system model. Compared with the previous version, the parameterization scheme of CLM4.5 is greatly improved, and it can describe various aspects of land surface processes, including surface

heterogeneity, biogeophysical processes, hydrologic cycles, biogeochemical processes, human impacts and ecosystem dynamic processes. To ensure data consistency when investigating the impacts of future precipitation on an ecosystem carbon budget, precipitation and temperature data of GFDL-ESM2 M under ISIMIP2b are also obtained. The data from 2006 to 2014 under RCP2.6 are blended into the historical period to achieve consistency for the same research period under ISIMIP3b.

2.3   Other datasets

To validate the performance of the reanalysis dataset, this study uses temperature data from HadISD developed by the Met Office Hadley Centre (Smith et al., 2011). HadISD has been checked and corrected for strict quality control and contains subdaily meteorological data from 9278 stations, covering the period from January 1931 to September 2021. In this study, 3 h near-surface temperatures during 1979–2020 are selected; for those stations providing hourly data, we obtain the 3 h data through temporal transformation.

The goal of the Global Land Data Assimilation System (GLDAS) is to process satellite- and ground-based observational data products using advanced land surface modeling and data assimilation techniques to generate optimal fields for land surface states and fluxes. The latest GLADS-2.2 assimilates CLSM outputs and GRACE/GRACE-FO satellite signals, which has produced a daily TWSA series with 0.25° spatial resolution during 2003–2020 (Save et al., 2016). Following the processing procedures of GRACE/GRACE-FO, we subtract the mean field of GLADS-2.2 from 2004 to 2009 and then obtain the daily, global TWSA series.

CERES (Clouds and the Earth's Radiant Energy System) is an important part of the Earth observation project, which has advanced the International Satellite Cloud Climatology

Project (ISCCP) and Earth Radiation Budget (ERB) observations. CERES involves a high level of data fusion. During the CERES period, the team processed data from 7 CERES instruments, 2 MODIS, 2 VIIRS and 20 geostationary imagers, and these were integrated to achieve climate accuracy in radiative fluxes from the top to the bottom of the atmosphere (Loeb et al., 2005). This study selects the net radiation flux at the top of the atmosphere from the SYN dataset in the CERES system, which blends CERES flux observations, MODIS-retrieved cloud characteristics and Earth synchronous satellite imaging products. The radiation data were subjected to a quality control process and calibration and were generated at 1° and hourly resolutions. In this study, we only use data from 2000 to 2020.

3. Methods

3.1 Deriving near-surface relative humidity and specific humidity

The C-C thermodynamic equation can be used to describe the nonlinear relationship between saturation vapor pressure (e_{sat}) and temperature (T) (Koutsoyiannis, 2012):

$$e_{sat}(T) = e_{s0}\exp\left[\frac{L_v}{R_v}\left(\frac{1}{T_0} - \frac{1}{T}\right)\right], \tag{1}$$

where T_0=273.16 K and e_{s0}=611 Pa are integration constants and L_v and R_v refer to the latent heat of vaporization (2.5×10^6 J kg^{-1}) and vapor gas constant (461 J kg^{-1} K^{-1}), respectively.

As the dew point temperature (T_{dew}) represents the temperature at which water vapor is saturated under constant water vapor content and pressure, it can be used to measure the actual water vapor pressure with the C-C relationship. Relative humidity can be deduced by substituting T_{2m} and T_{dew} into eq. (1) as RH=$e_{sat}(T_{dew})/e_{sat}(T_{2m})$.

The specific humidity (SH) refers to the ratio of the water vapor mass to the total air mass, which can be estimated by near-surface pressure (p) and T_{dew} (Simmons et al., 1999):

$$q = 0.622\frac{e_{sat}(T_{dew})}{p - 0.378e_{sat}(T_{dew})}. \tag{2}$$

3.2 Binning scaling between extremes and temperature

The binning scaling technique can describe the nonlinear relationship between different variables well and has been widely used to evaluate the response of precipitation extremes to global warming (Wasko et al., 2019). In each grid or station, the daily precipitation intensity and the same-day temperature data are paired and placed into 12 bins by clustering temperature such that the near-surface temperatures are similar in each bin. Within each bin, precipitation intensities are ranked to determine the five largest pre-

cipitation events with intensities exceeding the 99th percentile extreme, and the mean temperature of the events in this bin is used to represent local temperature.

The differential form of the C-C relationship can be expressed as (Yin et al., 2021a):

$$\frac{de_{sat}}{e_{sat}dT} = \frac{L_v}{R_v}\frac{1}{T^2}. \tag{3}$$

As convective intensity is closely governed by atmospheric moisture availability, in the absence of relative humidity change, an exponential regression could be established in linking precipitation rates to the near-surface temperature variation δT (Yin et al., 2021b):

$$P_2 = P_1\big(0.01\alpha_p + 1\big)^{\delta T}, \tag{4}$$

where P_1 and P_2 indicate different precipitation extremes averaged by the five largest events in each bin, and α_p denotes the scaling rate.

Numerous studies have classified the scaling types of precipitation extremes into three categories: monotonic increasing, monotonic decreasing and a hook structure. To detect the scaling types, the temperature at which precipitation peaks, T_{pp}, is identified from the locally weighted regression smoothing (LOWESS) approach. If T_{pp} is located in the highest (or lowest) temperature bin, the scaling type is monotonically increasing (or decreasing). Otherwise, the scaling type is identified as having a hook structure. In a hook structure, the regression curve is fitted only up to T_{pp} (Yin et al., 2018, 2021a). To investigate the impacts of atmospheric thermodynamics and dynamics on precipitation extremes, we also estimate the temperature scaling rate of TCWV, CAPE and RH during precipitation extremes.

Both the MSWEP-V2 and ERA5 datasets are used to characterize the scaling relationship between multitemporal precipitation extremes and daily average temperature, and the LOWESS method is used to identify the scaling types. When evaluating the temperature scaling of subdaily precipitation extremes, we still employ the daily average temperature because the subdaily temperatures are highly influenced by boundary layer activities and are not suitable for measuring the atmospheric moisture content (Lenderink and Van Meijgaard, 2008). In previous climate change impact assessments, only precipitation events with rates over 0.1 mm were considered when defining an extreme event (e.g., Yin et al., 2018; Sullivan et al., 2020), which is a "wet-event" definition scheme. More recently, a few studies have found that the occurrence of precipitation events has been altered due to climate change and human activities. As the wet-event definition method may achieve results contrary to the real situation (Appendix Figure S1, https://link.springer.com), some studies suggest that all data should be used in defining an extreme precipitation event, which is called an "all-event" scheme (Schär et al., 2016). In this study, we

adopt these two definitions to estimate the 99th percentile precipitation in temperature bins and then investigate the response of precipitation extremes to climate change.

3.3 Spatiotemporal identification of three-dimensional precipitation events

Previous studies have usually examined the changes in precipitation extremes at a given time scale (e.g., daily or hourly). However, severe precipitation events that cause large amounts of damage usually exhibit a certain space-time continuity. For example, precipitation over a longer duration or larger coverage area is likely to trigger more severe flood hazards and socioeconomic losses (Dwyer and O'Gorman, 2017; Blöschl et al., 2020). In this study, we assume precipitation to be a three-dimensional event (longitude-latitude-time) and examine its changes. The three-dimensional precipitation events are identified by employing the following steps.

(1) Identifying precipitation patches. A minimum precipitation threshold P_0 (0.1 mm/3 h in this study) is set to identify the wet-day state of each grid. For each time step t, global precipitation events are clustered into several patches with consideration of spatial continuity, and then the matrix of patches (L) is obtained.

(2) Identifying the temporal continuity of precipitation patches. As precipitation events with wide coverage and long duration receive more attention in the field of climate change, we omit small patches that cover less than the minimum precipitation area A_0 (five grids in this study). As shown in Figure 2, it is assumed that there are precipitation patches E_{t-1} and E_t at $t-1$ and t at two adjacent time steps, respectively, and their overlap area A on the two-dimensional projection plane is calculated. If $A>A_0$, E_{t-1} and E_t are clustered into the same precipitation event; otherwise, they belong to different precipitation events (Xu et al., 2019).

(3) Extracting three-dimensional precipitation events. We repeat step (2) until the final time step, and then all the precipitation patches with spatiotemporal continuity are uniquely labeled.

The average intensity (I_E) of three-dimensional precipitations is calculated as follows:

$$I_E = \frac{\sum_{t=1}^{NT}\left(\sum_{j=1}^{N}\omega_j \cdot G_{t,j} \cdot P_{t,j}\right)}{NT\sum_{j=1}^{N}\omega_j},\tag{5}$$

where NT and N denote the lasting time and covering grid number, respectively; ω_j denotes area weights at different latitudes, and $P_{t,j}$ is precipitation intensity at time t and grid j; $G_{t,j}$ is an indicator function, when $G_{t,j} \geq P_0$, $G_{t,j}=1$; otherwise, $G_{t,j}=0$.

3.4 Assessing the response of the ecosystem carbon budget to precipitation events

GPP, TER and NEP are often used to evaluate the carbon budget processes of an ecosystem. Chlorophyll fluorescence rereleases energy at longer wavelengths after light absorption during vegetation photosynthesis, which can directly reflect the electron transfer rate during the light reaction process, and the electron transfer rate is regulated by the carbon reaction rate of photosynthesis. Therefore, chlorophyll fluorescence remote sensing technology has been regarded as one of the most important breakthroughs in the field of vegetation remote sensing in the last decade, and SIF is also used as an ideal proxy for GPP during plant photosynthesis (Zhang et al., 2020). We first calculate the mean values of SIF on clear days (delayed 1–2 days after precipitation events) and during the whole study period, with the aim of evaluating the impact of precipitation on ecosystem carbon assimilation. To analyze the SIF response to different precipitation intensities, we classify the precipitation events during the warm season into three bins (segmented by the 10th and 50th percentile intensities). Finally, in each intensity bin, we examine the differences in the mean values of
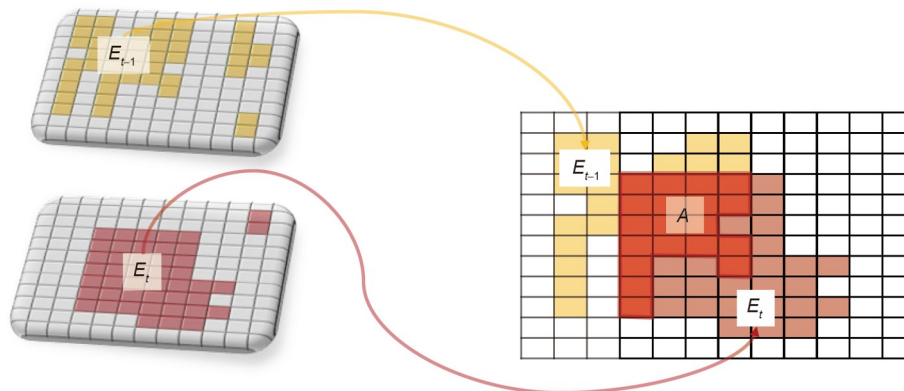

Figure 2 Schematic for identifying three-dimensional precipitation events.

SIF on clear days after precipitation events and on all clear days.

To analyze the response of the ecosystem carbon budget to precipitation, we further use the measurement data (soil moisture, precipitation, air temperature, GPP, TER, and NEP) from 69 flux stations across the globe. At each site, the warm season is defined as days when running 7-day mean temperatures are higher than the 60th percentile of the daily temperatures. We sort the observed daily precipitation and temperature at the flux tower sites into 10×10 percentile bins at each site and calculate the mean anomalies of GPP, TER, and NEP in those bins across the 69 sites. The binning method can well describe the relationship between multiple variables; please refer to Zhou et al. (2019) for detailed processing procedures. To comprehensively examine the effects of different hydrometeorological factors on the carbon budget, air temperature is further replaced by soil moisture and TWS for the above binning analysis, using both daily TWS data from GLADS-2.2 and monthly TWSA series from the GRACE/GRACE-FO dataset. Finally, with carbon flux data simulated by the CLM4.5 model under ISIMIP2b, we assess the impact of different precipitation intensities on the carbon budget under climate change.

4. Results and discussion

4.1 Response of water-heat-carbon flux to precipitation extremes

By using the empirical distribution method, the threshold for precipitation extremes (i.e., 90th percentile of daily precipitation intensity) during 1979–2020 is estimated by the ERA5 dataset, and then the spatial distribution of global precipitation extremes is presented. Tropical oceans have higher precipitation extremes, and the intensity of precipitation extremes in coastal lands is usually higher than that in inland areas, suggesting the important role of the ocean in supplying moisture for precipitation generation (Figure 3a). To analyze the response of the land-atmosphere system to precipitation extremes, we calculate the average difference of each factor during heavy precipitation (precipitation intensity exceeding the 99th percentile) and non-precipitation days (precipitation intensity less than 1 mm d^{-1}). The considered hydrometeorological variables mainly involve three types: (1) humidity factors, including RH, SH, TCWV and MFC; (2) energy factors, including sensible and latent heat flux (upward positive), CAPE and CIN; and (3) atmospheric dynamic factors, represented by vertical velocity (upward positive). Humidity, energy and atmospheric dynamic factors play key roles in convection and precipitation generation in the atmospheric boundary layer, which are highly correlated, so it is often difficult to identify the driving forces behind individual factors on precipitation. Therefore, this study comprehensively analyzes their impact on precipitation. As shown in Figure 3, there are significant differences in these water-heat variables between precipitation and non-precipitation conditions. During precipitation extremes, MFC is enhanced (Figure 3b), indicating that the suction function of the surrounding water vapor is an important factor feeding precipitation extremes. Land and ocean show different heat exchange patterns; precipitation is accompanied by phase transition, the land boundary layer releases a large amount of latent heat (Figure 3e), and the sensible heat flux transmitted from the surface to the atmosphere is weakened (Figure 3d), thus cooling the near-surface temperature of most global lands (Figure 3f). The ocean provides sufficient moisture for atmospheric convection, and the latent heat even decreases in some sea areas during precipitation extremes (Figure 3e). As a result, the ocean becomes the main heat source, and the heat transmitted to the atmosphere increases in most sea areas (Figure 3d), thus warming the air temperature above the ocean (Figure 3f). CAPE is an important indicator for describing atmospheric thermal characteristics, representing the maximum potential energy of air blocks for convection, which is often used to measure the instability of atmospheric stratification and the development of convection intensity (Yin et al., 2022). CIN represents the energy that prevents air blocks from rising from the ground to the height of free convection. A high CIN indicates that the atmosphere tends to be stable, which hinders the generation of thunderstorms and is often regarded as an energy indicator opposite to CAPE. As shown in Figure 3j, CAPE (CIN) during precipitation extremes increases (decreases), and the vertical velocity is significantly enhanced (Figure 3l), suggesting that strong energy transport and upward air movement contribute to enhanced precipitation. The air updraft process provides a large amount of water vapor to the middle and upper atmosphere, resulting in increases in both RH and SH (Figure 3g–3h), and contributes to TCWV enhancement (Figure 3i). The increase in atmospheric water vapor content further promotes increases in convection and in the formation of precipitation extremes, suggesting a complex feedback mechanism between precipitation and the water-heat exchange process of the land-atmosphere-ocean system. The feedback process between water-heat variables and precipitation extremes on land is generalized in Figure S2.

After deriving the warm season (i.e., three continuous months of the highest temperature months) for the global grids (Figure S3a), we calculate the average difference between the SIF values of clear days after precipitation events and the SIF values of dry days during the warm season. Higher GPP often occurs after precipitation events (Figure 3c), suggesting the important role of precipitation in providing water conditions for vegetation photosynthesis and ecosystem carbon assimilation. Figure S4 presents the dif-
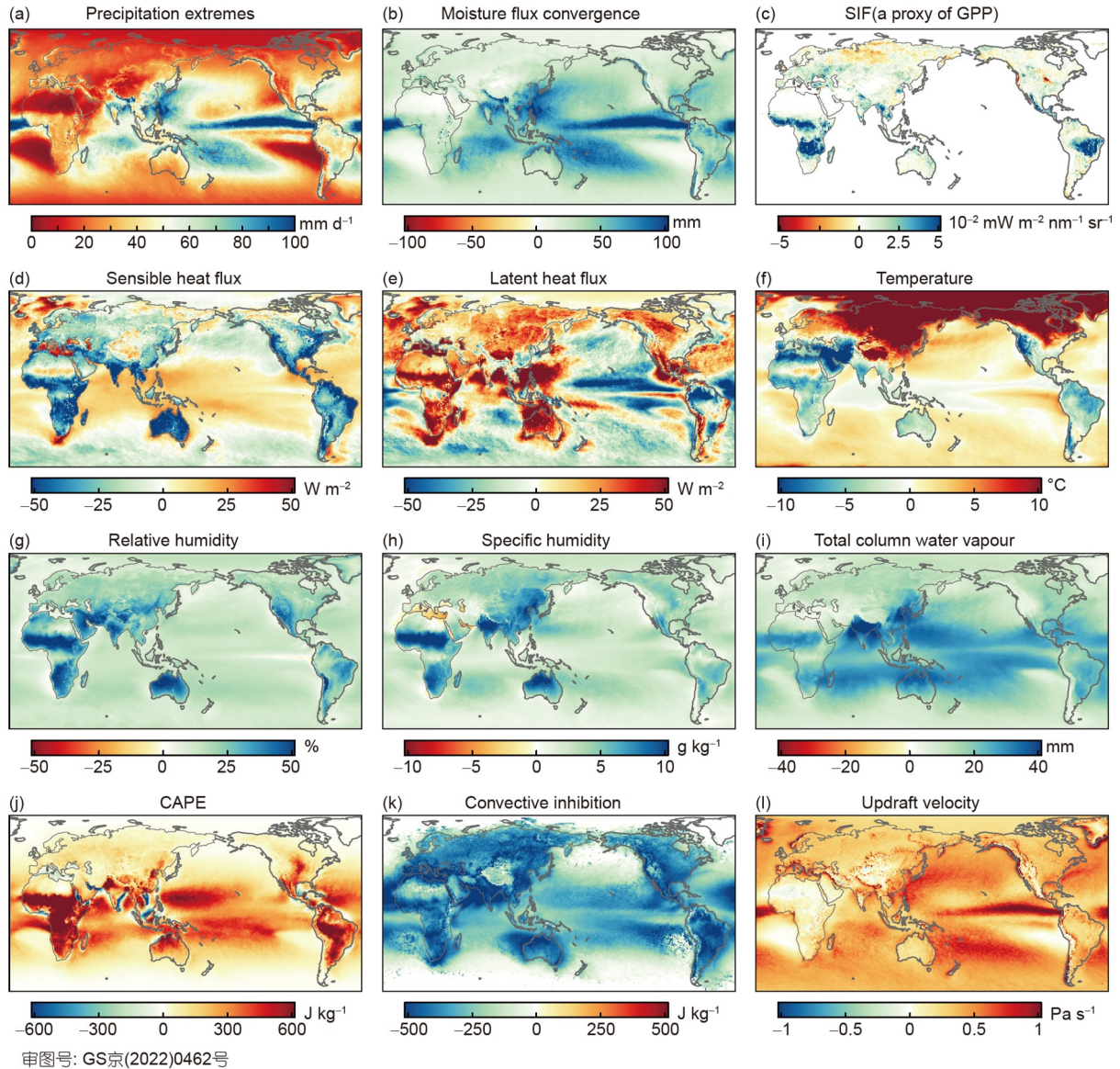
Figure 3 Global daily precipitation extremes and their impacts on water-heat-carbon variables. (a) Spatial distribution of global 99th percentile daily precipitation extremes. (b), (d)–(l), Anomalies of variables in precipitation extremes. (c) Differences in average SIF values on clear days after precipitation and on all non-precipitation days.

ferences between the mean SIF of clear days after precipitation events under different intensities and the mean SIF of all clear days during the warm season. During a precipitation event, although the daily precipitation intensity only reaches the 10% threshold of the cumulative distribution function, SIF in most regions of the globe is higher than the average state (Figure S4a), which further confirms the important role of precipitation on vegetation photosynthesis. In some alpine regions, the SIF after precipitation is lower than the average state because snow and glaciers may provide the necessary water conditions for vegetation, and further precipitation may exceed the required water for vegetation growth. Precipitation events in this region may also be accompanied by low radiation and cold temperatures,

which can negatively affect vegetation growth. When the daily precipitation increases to a certain intensity, SIF will not continue to increase with increasing precipitation. Under some conditions over humid areas, SIF may decrease with increasing precipitation intensity (Figure S4b, S4c), implying that a linear function cannot be directly used to measure the relationship between precipitation and ecosystem productivity; therefore, a complex nonlinear response relationship should be considered. Following the method illustrated in Section 3.4, Figure 4 presents the results of the response pattern for the carbon budget to precipitation considering a 1-day lag. Compared with precipitation, air temperature shows stronger effects on the ecosystem carbon budget. Plant photosynthesis and respiration reach an average state only
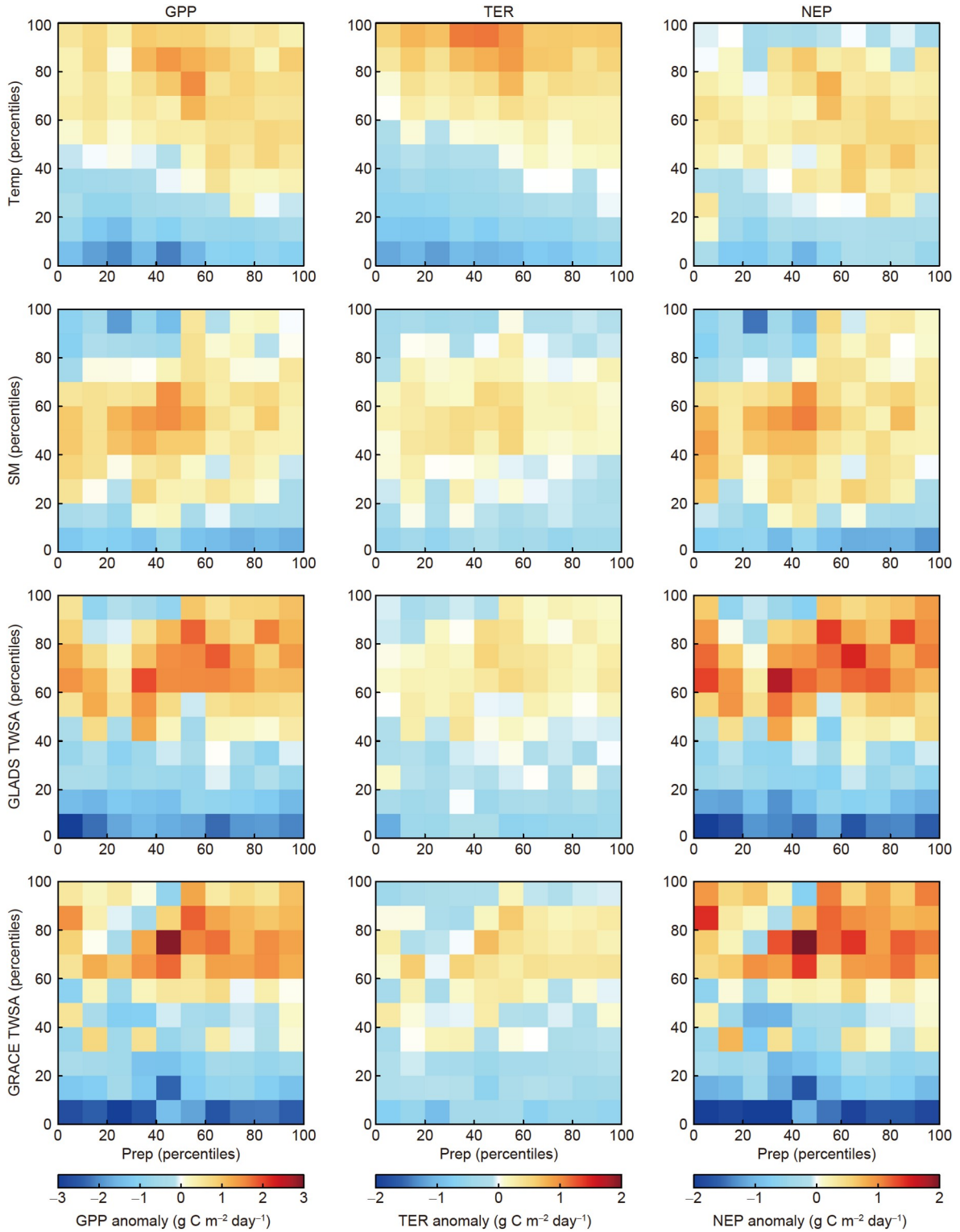
Figure 4 Impacts of precipitation, temperature, soil moisture and TWS on the ecosystem carbon budget. The first, second and third columns represent anomalies of GPP, TER and NEP, respectively. The abscissa represents precipitation percentiles, while the ordinates of each row indicate temperature, soil moisture, TWS from GLADS, and TWS from GRACE. The binning probability is averaged from 69 global flux tower results.

when the air temperature rises to a certain degree. When soil moisture is too high (e.g., over 80% percentile), the carbon exchange rate between the vegetation and atmosphere is

significantly reduced, which may be due to constraints to the root function caused by waterlogging stress, thus limiting the uptake of water and nutrients by vegetation. These conclu-

sions are also confirmed by two TWS datasets as well as by 2-day lags (Figure S5). It is further found that moderate precipitation can promote photosynthesis and respiration rates, while excessive precipitation (e.g., over the 90th percentile) may reduce NEP. When soil moisture is lower than the 20th percentile, NEP will be weakened by either a very low (less than the 30th percentile) or very high (heavier than the 70th percentile) level of precipitation.

When soil moisture reaches the 40th–50th percentile, heavy precipitation may reduce NEP, but the NEP is still higher than the average state. The above results show that the ecosystem carbon budget is affected by multiple factors, and it can be evaluated well only when multivariate processes are taken into consideration. Generally, vegetation growth and carbon assimilation lead precipitation, temperature, soil moisture, and the TWS range to be in the average state (40th–70th percentile); extremely cold/hot or dry/wet conditions weaken the carbon assimilation capacity of the ecosystem.

## 4.2 Spatiotemporal evolution pattern of global precipitation extremes

The global long-term trends in the intensity of daily and subdaily precipitation extremes are estimated by using the MSWEP-V2 and ERA5 datasets, respectively. First, the daily maximum 3 h (1 h) precipitation and daily total precipitation are calculated based on the MSWEP-V2 (ERA5) dataset. The daily precipitation extremes in each year are extracted by the 99th percentile of the daily series, and subdaily extremes are represented by the 99th percentile of the daily maximum 1 h (ERA5) or 3 h (MSWEP-V2) precipitation intensity. Finally, the long-term trend for the annual extremes is investigated in each grid. In the past 40 years, the intensity of precipitation extremes has significantly increased in most areas of the globe (Figure 5a, 5d). The trends in some regions might differ from different datasets; the MSWEP-V2 dataset shows that the precipitation intensity over the tropical ocean is decreasing, while the ERA5 dataset suggests an overall tendency toward intensification of precipitation extremes. Figure 5e and 5f shows that the trend in the annual average duration of global precipitation events is shortening, suggesting that the temporal distribution of precipitation events has been altered and precipitation events are becoming more concentrated.

To further explore the spatiotemporal distribution of precipitation extremes, three-dimensional precipitation events are identified by the MSWEP-V2 dataset (1979–2017), and then the monthly occurrence, average coverage grids and intensity over ocean and land are calculated. As shown in Figure 6, more three-dimensional precipitation events occur over the ocean than over land, and the coverage area (intensity) over the ocean is larger (lower) than that over land.

In the past 40 years, the average coverage area (frequency and intensity) of three-dimensional precipitation events over land and ocean has decreased (increased) significantly, further confirming that the spatiotemporal distribution of global precipitation extremes is more concentrated and that short-duration, heavy precipitation events have occurred more frequently.

4.3 Temperature scaling of global precipitation extremes and hook structures

Figure 7a–7d presents the scaling types of precipitation extremes as well as the T_{pp} of the hook structure under the all-event definition. High latitudes generally show a monotonic increasing scaling type, and the middle latitudes usually have a hook structure. Tropical lands usually show a monotonically decreasing scaling type, while tropical oceans generally have a hook structure or a monotonically increasing type. Compared with the precipitation extremes at the subdaily (1 or 3 h) scale, the daily precipitation extremes are more likely to exhibit a monotonic increasing type. Comparing the results of the all-event and wet-event schemes, it is found that the scaling structures of precipitation extremes in tropical land regions show large differences (Figure S6). For example, in the Indian Peninsula, Indochina Peninsula, parts of Africa, and northern Australia, precipitation extremes under the wet-event (all-event) definition show a monotonic decreasing (hook) type, implying the important role of different definitions of precipitation extremes on scaling structures. The scaling rates of multitemporal precipitation extremes in high latitudes are usually lower than 6.8% °C^{-1} (sub-CC scaling), while some regions of the mid-latitudes show a scaling rate of approximately 6.8% °C^{-1}. Tropical lands generally show a negative scaling rate, while some areas in the tropical ocean show a higher scaling rate (over 20% °C^{-1}), which may be explained by the greater amount of moisture present in the ocean, but moisture transport to land is constrained. The scaling rates of daily and subdaily precipitation extremes are similar over most regions of the globe, albeit with large degrees of uncertainty and spatial heterogeneity. Under the wet-event (all-event) definition, central America, southern Africa, the Indian Peninsula, the Indochina Peninsula and northern Australia show negative (positive) scaling rates for precipitation extremes. In south-central Australia and some regions of east and middle Asia, the wet-event and all-event definitions show near C-C and super C-C scaling rates, respectively. We further assess the scaling rates of precipitation extremes at different temporal scales by using HadISD temperature and MSWEP-V2 precipitation and find very few differences from the reanalysis results (Figure S7). The above results show that the scaling types and rates are similar under multitemporal precipitation extremes, while different extreme definition methods have
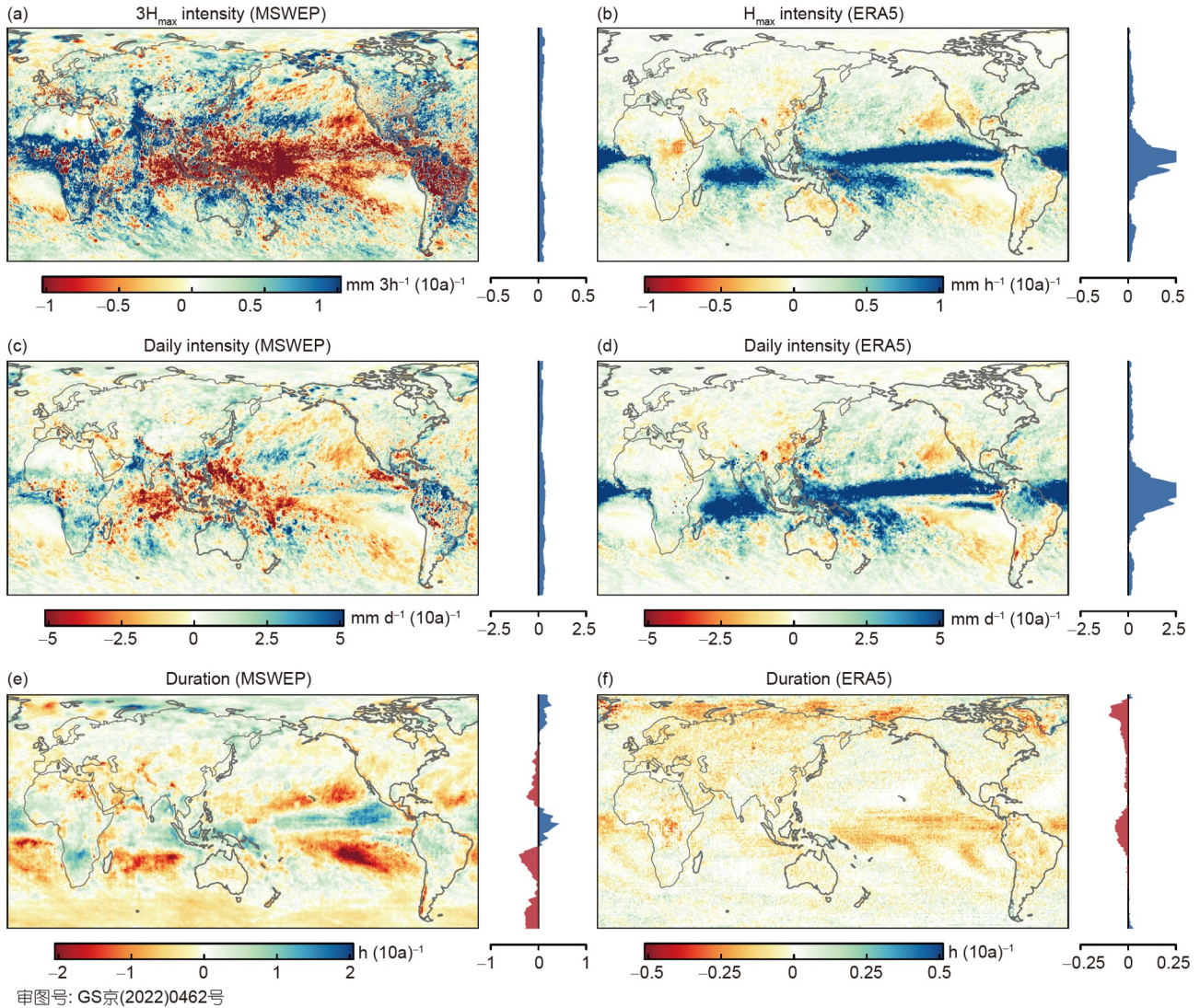
Figure 5 Global trends in the intensity and duration of multitemporal precipitation. (a), (b), Subdaily precipitation intensity; (c), (d), daily precipitation intensity; (e), (f), precipitation duration. The right bar indicates average trends in each latitude band.

significant impacts on the response pattern.

According to the C-C thermodynamic relationship, the saturated vapor pressure in the atmosphere nonlinearly increases with increasing temperature. Why do global precipitation extremes exhibit a hook structure? To illuminate this issue, the trends in TCWV, CAPE and RH for daily precipitation events exceeding the annual 99th percentile are estimated. The CAPE and TCWV in precipitation extremes increased significantly (Figure 8c, 8d), while the RH in most regions of the globe showed a decreasing trend (Figure 8a, 8b). W further estimated the temperature scaling rates of RH, CAPE and TCWV and found that CAPE usually had a scaling rate of over 6.8% °C^{-1} (Figure 8e), suggesting its positive role in intensifying precipitation extremes. The TCWV shows sub-C-C scaling and even a negative rate in the tropics (Figure 8g), which is because the actual atmospheric vapor pressure is determined by both e_{sat} and RH.

Although e_{sat} increases with warming temperature at a rate of C-C scaling, the RH decreases significantly with temperature in a hotter environment (Figure 8f). The constraints due to the water moisture supply in a hot environment reduce the scaling rate of TCWV and thus limit precipitation intensification, suggesting that the hook structure might be attributed to dynamic constraints.

To explore the influences of global precipitation extremes on the terrestrial water cycle, we further estimate the long-term trends in several variables (i.e., daily average top of atmospheric net flux, daily near-surface temperatures, and monthly TWS of GRACE/GRACE-FO). Under the impact of the "greenhouse effect", the atmospheric radiation budget has been altered, and global net radiation has increased significantly (Figure 8h). As a result, global near-surface temperatures are greatly warming (Figure 8i), and the atmospheric water vapor holding capacity is therefore in-
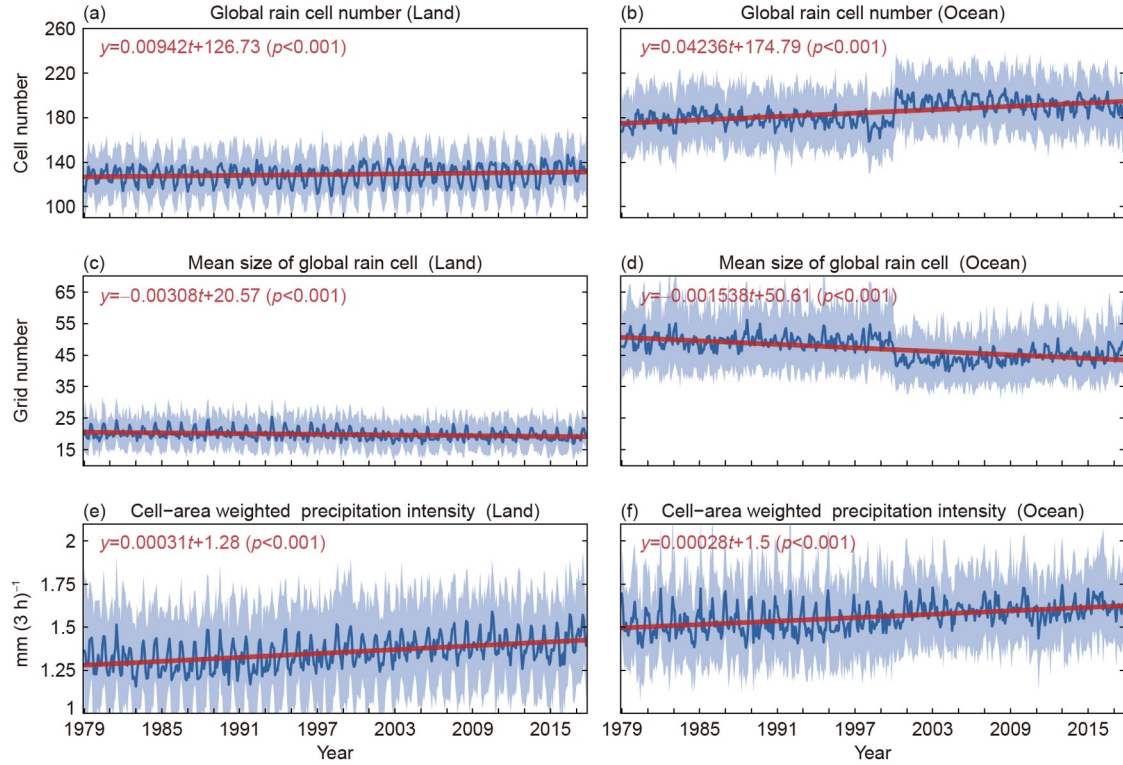
Figure 6   Interannual changes in the pattern of global three-dimensional precipitation events over land and ocean. The blue solid line and shading indicate monthly average values and 95% confidence intervals, respectively, and the red line represents trends.

creasing. Despite the dynamic constraints, precipitation extremes over most regions of the globe are still increasing (Figure 5). In the context of global warming, the TWS over most regions of the globe shows a drying tendency (Figure 8j), which seems to be contrary to the intensification of precipitation extremes. To investigate this issue, we estimate the Spearman correlation coefficient between TWSA (from both GLDAS and GRACE/GRACE-FO) and near-surface temperatures in the warm season and plot the binning probability averaged from global grids. We find that both monthly and daily TWSA have a negative correlation with near-surface temperatures globally (Figure S8). Increases in precipitation extremes do not imply a wetting tendency on land, and most parts of the globe are becoming dry, which might be due to the comprehensive influences of soil, evapotranspiration, vegetation physiology, rapid urbanization, industrial and agricultural water withdrawal, water diversion, and overextraction of groundwater (Wang et al., 2021).

4.4   Projections of global precipitation and impacts on the carbon budget

The spatiotemporal evolution pattern for precipitation is particularly complex. With the outputs of five GCMs under ISIMIP3b, we estimate the changes in daily precipitation extremes (99th percentile) late in this century (2071–2100) with the baseline of the historical period (1985–2014) under

three SSPs. All 15 scenarios projected a significant intensification in global precipitation extremes in the future climate. Precipitation extremes exhibit the highest rate of increase (15–40%) under SSP585; SSP126 shows a relatively lower rate of increase, but most global regions still have an increase rate of over 10% (Figure 9).

Why do precipitation extremes increase under the constraint of a hook structure? To probe this issue, Figure 10 presents future changes in the scaling type projected by the GCMs. As the scaling types can be classified into three categories during both historical and future periods, there are nine possible categories for future changes. For example, 'D-H' indicates that the scaling type changes from a monotonic increasing type (D) to a hook structure (H) under climate change (Figure 10). As shown in Figure 10, precipitation extremes in most parts of the globe present a hook structure during both historical and future periods, and their T_{pp} values are projected to increase by 1–5°C by the end of this century. These results indicate that the scaling structures are unstable and can dynamically shift with climate warming. Despite being constrained by atmospheric dynamics, the precipitation intensity at T_{pp} increase with shifts in hook structures. Portions of the tropics show a monotonic decreasing type during both historical and future periods, but the precipitation extremes are still projected to increase. This is because the D-type scaling curve shifts toward the warming side in future climates, resulting in an intensification in precipitation
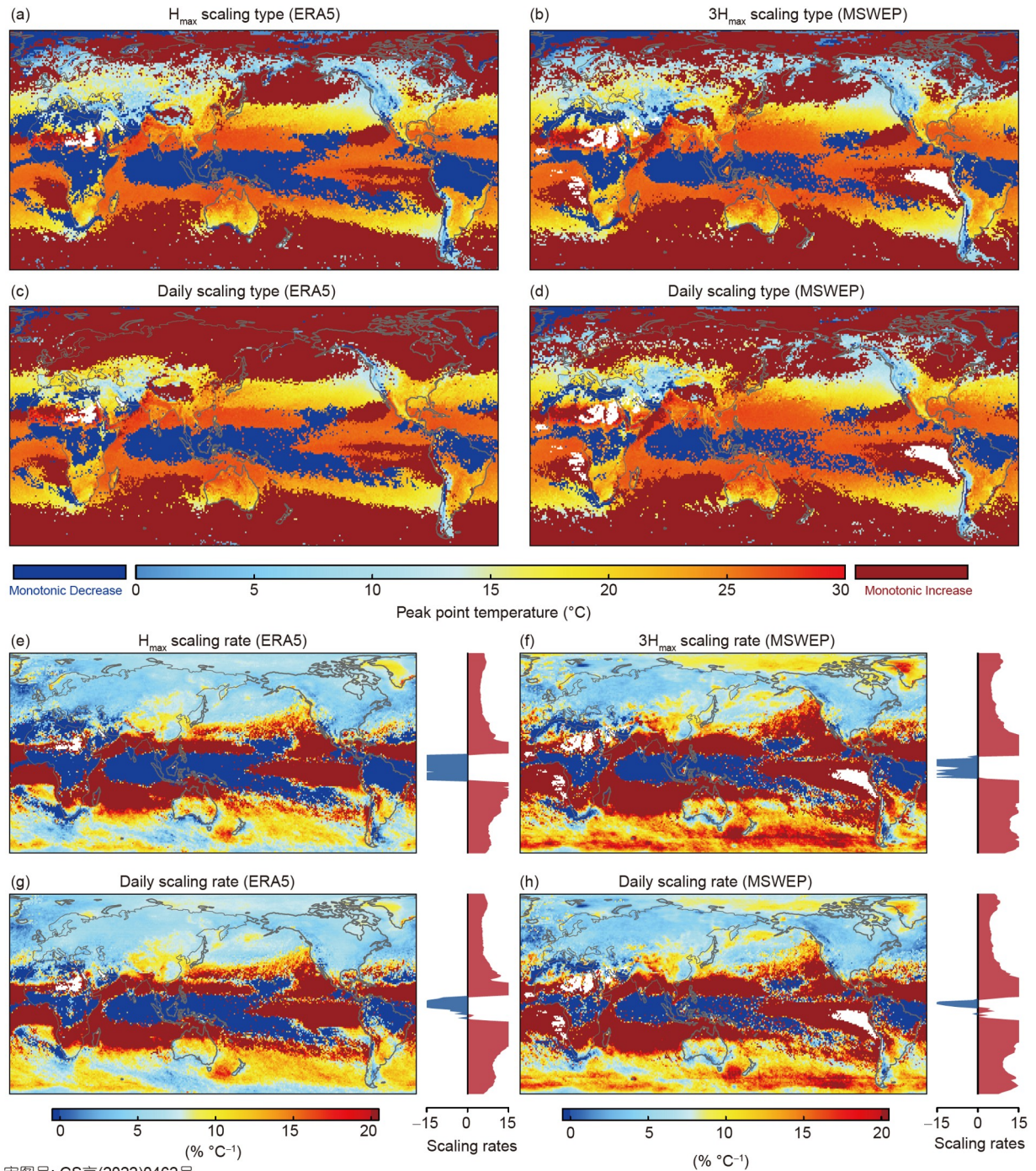
Figure 7 Scaling structure, peak point temperature and scaling rate of global precipitation extremes under the all-event definition. (a)–(d), Scaling structure and peak point temperature of subdaily ((a), (b)) and daily ((c), (d)) precipitation extremes. (e)–(h), Scaling rate of subdaily ((e), (f)) and daily ((g), (h)) precipitation extremes. The right bar indicates the average scaling rate of each latitude band.

extremes for the coldest temperatures (T_{pp} of the D-type curve). Although the results are accompanied by uncertainty originating from the different GCMs (e.g., UKESM1-0-LL usually projects a stronger changing signal), the main conclusion of future precipitation intensification is robust.

To investigate the impact of future precipitation on the ecosystem carbon budget under climate change, we quanti-

fied the response of GPP, TER, NEP, autotrophic respiration (Raut), and soil heterotrophic respiration (Rhet) to precipitation by using outputs from the Earth system model (ESM) and community land surface models. Due to the lack of daily carbon flux data under the model simulations, we conduct the analysis at a monthly scale. First, the warm seasons in each grid are identified by using the historical
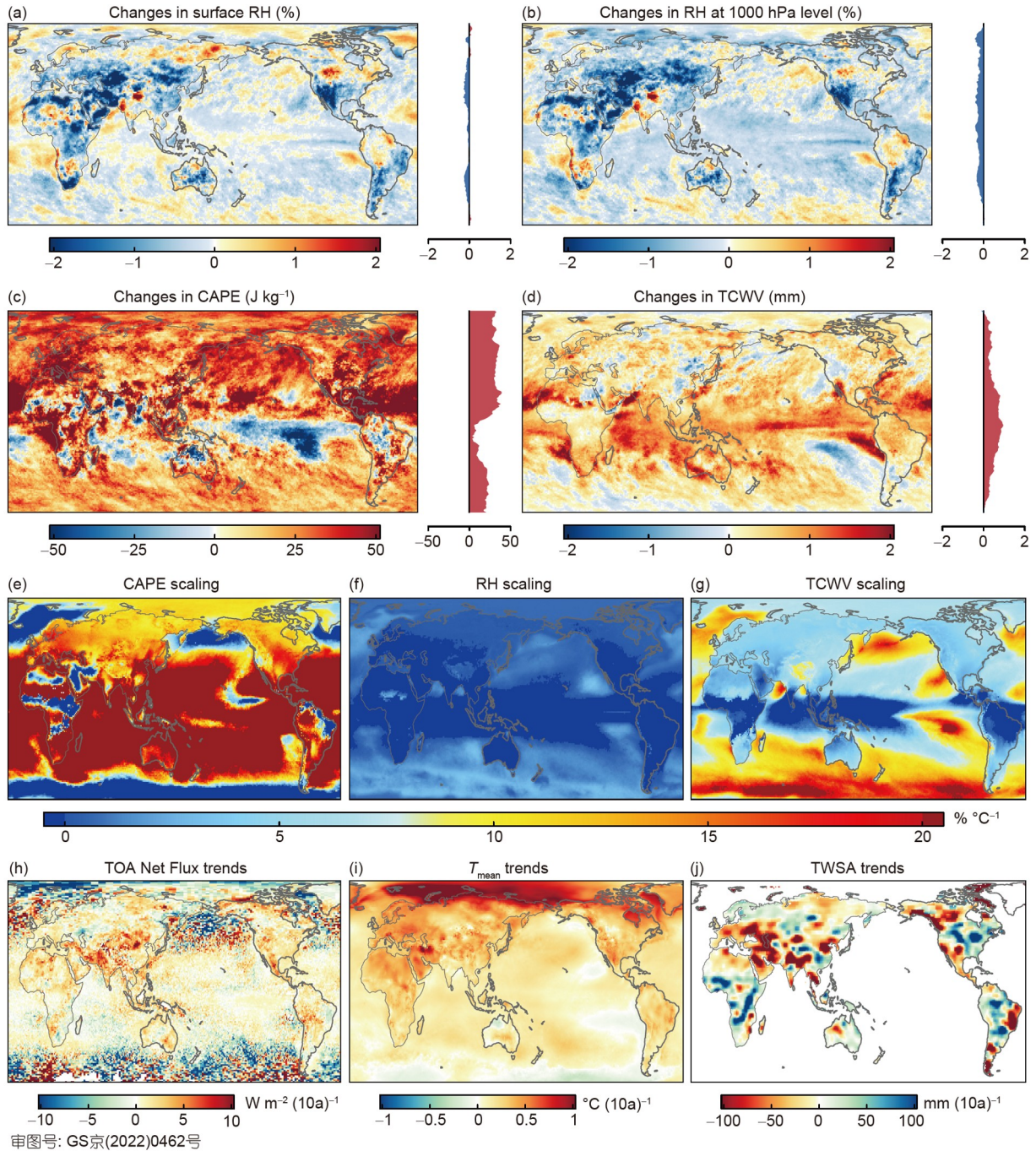
Figure 8   Trends and scaling rates of different meteorological variables during 1979–2020. (a)–(d), Trends in relative humidity, CAPE and TCWV during precipitation extremes. (e)–(g), Scaling rate of near-surface temperature with CAPE, relative humidity and TCWV. (h)–(j), Trends in top of atmospheric net flux, near-surface temperature and terrestrial water storage.

temperature outputs of GFDL-ESM2 M (Figure S3b), and then the carbon flux anomalies under two different water stresses are calculated under two RCPs. Figure 11 (Figure S9) presents the anomaly of carbon budget fluxes in months with precipitation exceeding the 90th (below the 10th) percentile with reference to the overall warm season. It is found that photosynthesis and respiration of ecosystems are higher in most regions of the globe when precipitation is abundant, except in a few alpine, plateau or coastal areas. Net eco-

system productivity is higher under moderate precipitation conditions across most regions of the globe, but it is lower in some coastal or humid regions, which may be caused by differences in water conditions arising from regional topographic and climatic conditions. To test the sensitivity of different precipitation threshold effects on the carbon budget, Figures S10 and S11 present the carbon budget flux anomalies under conditions in which the high/low precipitation conditions are defined by 99 and 1%, respectively.
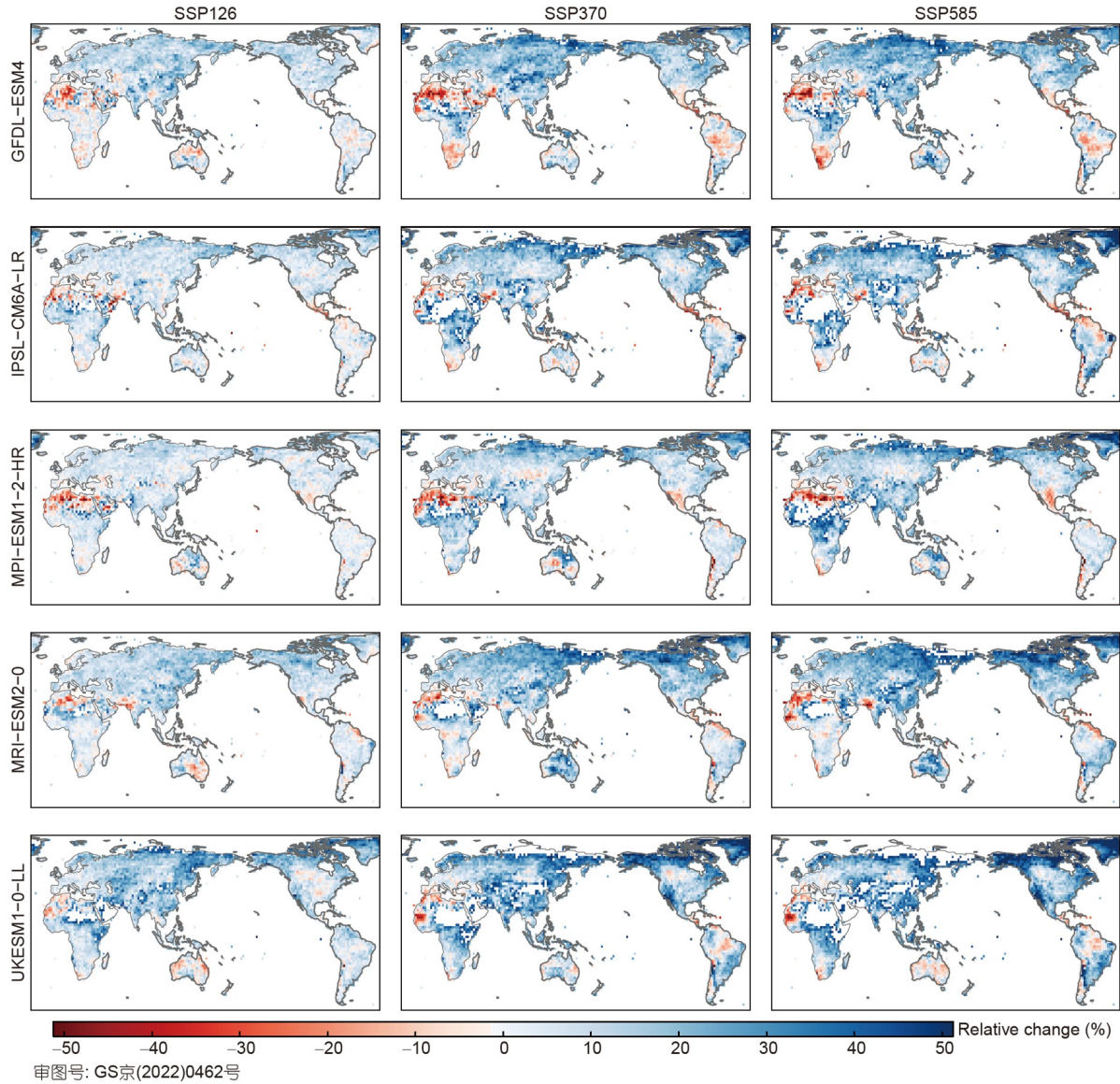
Figure 9   Relative changes in precipitation extremes by the late century under three SSPs.

It is found that the main conclusions still hold true, but the differences in NEP are more significant than those under the 90/10% conditions. Moreover, the different RCPs have very few impacts on the ecological effects of precipitation, and there is no significant difference in the response of the ecosystem carbon budget to precipitation conditions in the historical and future periods. Overall, the CLM4.5 projects that moderate precipitation contributes to carbon assimilation in ecosystems, and the response of the carbon budget to precipitation is stable under climate change.

5.   Conclusions

This paper utilizes MSWEP-V2, ERA5 atmospheric re-analysis, GCM outputs, CLM4.5 outputs, HadISD mea-

surements, GLADS system, GRACE/GRACE-FO dataset, global flux tower measurements, a machine-learning-generated dataset, and radiation from the CERES project. We first assess the response of the water-heat-carbon flux to precipitation extremes and examine the impacts of hydro-meteorological variables (e.g., temperature, precipitation, soil moisture and TWS) on the ecosystem carbon budget. We then investigate changes in the intensity and duration of precipitation extremes at different time scales and examine the frequency, coverage area and average intensity of three-dimensional precipitation events over global lands and oceans. Based on the extended C-C relationship, we identify the scaling structure of multitemporal precipitation extremes and their T_{pp} and explain hook structures by examining the impacts of vapor and energy factors (i.e., RH, CAPE and TCWV) on precipitation. Using projections from five GCMs
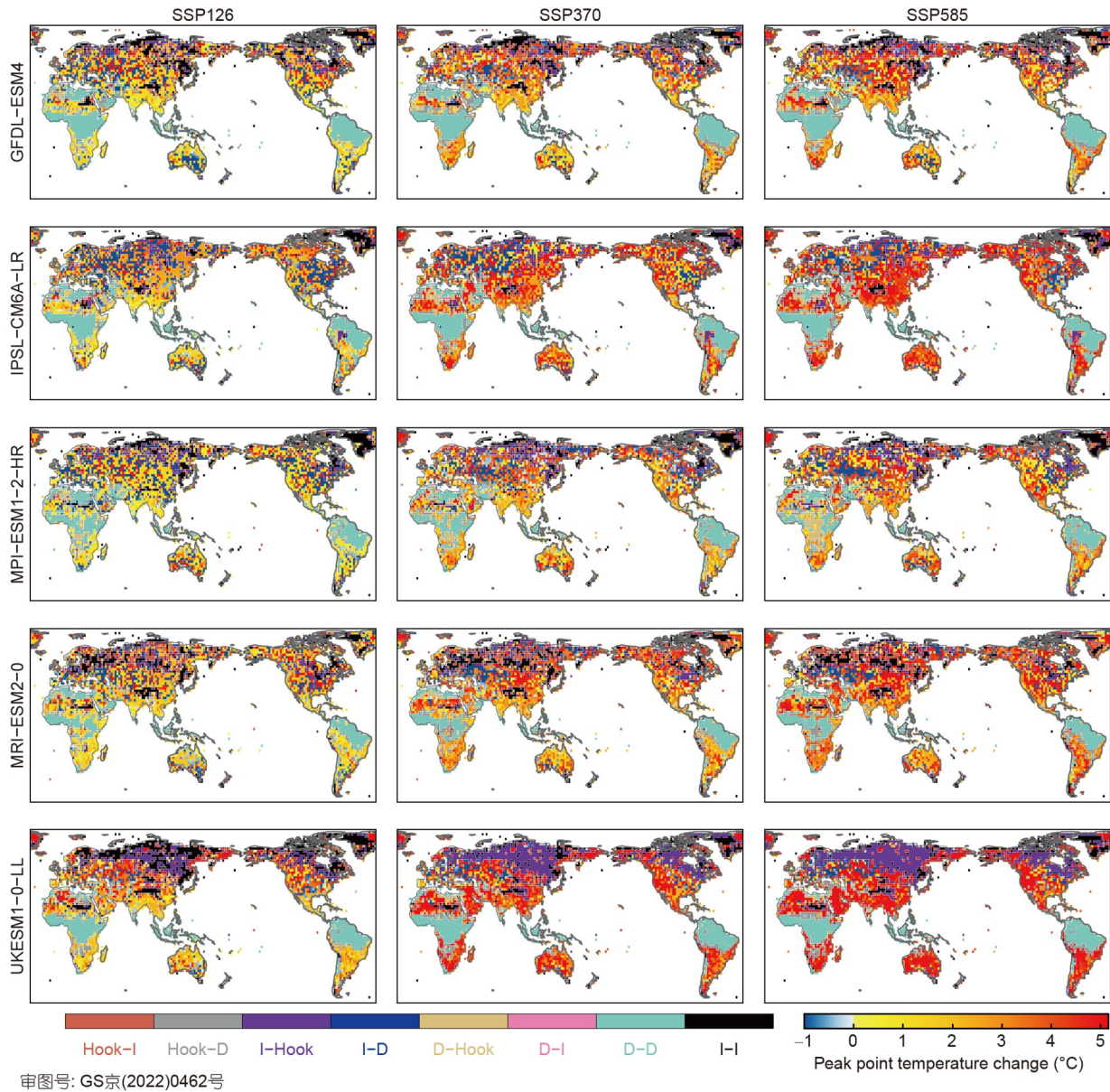
Figure 10   Changes in scaling structures and peak point temperatures of precipitation extremes under three SSPs.

and three SSPs under ISIMIP3b, we project the shifts in the hook structures and their impacts on precipitation extremes and finally investigate the impact of precipitation on the ecosystem carbon budget by using outputs from the CLM4.5 model.

This study investigates the thermodynamic driving mechanisms of global precipitation extremes and ecohydrological effects and finds complex feedback mechanisms between precipitation and water-heat transport in the land-vegetation-atmosphere system. Precipitation provides important water conditions for ecosystem productivity and carbon assimilation, but a severe rain event can reduce ecosystem productivity. The carbon budget processes are governed by multiple factors, such as temperature, soil

moisture and TWS, and temperature plays a dominant role. In the past 40 years, the average coverage area (frequency and intensity) of three-dimensional precipitation events over lands and oceans has decreased (increased) significantly, further confirming that the spatiotemporal distribution of global precipitation extremes has become more concentrated and that short-duration heavy precipitation events have occurred more frequently. The precipitation extremes in high latitudes are usually of a monotonically increasing scaling type, while those of the middle-latitude regions show a hook structure. Tropical land regions generally have a monotonically decreasing scaling type, while the tropical oceans show a hook structure or a monotonically increasing scaling type. In high- and mid-latitude regions, precipitation ex-
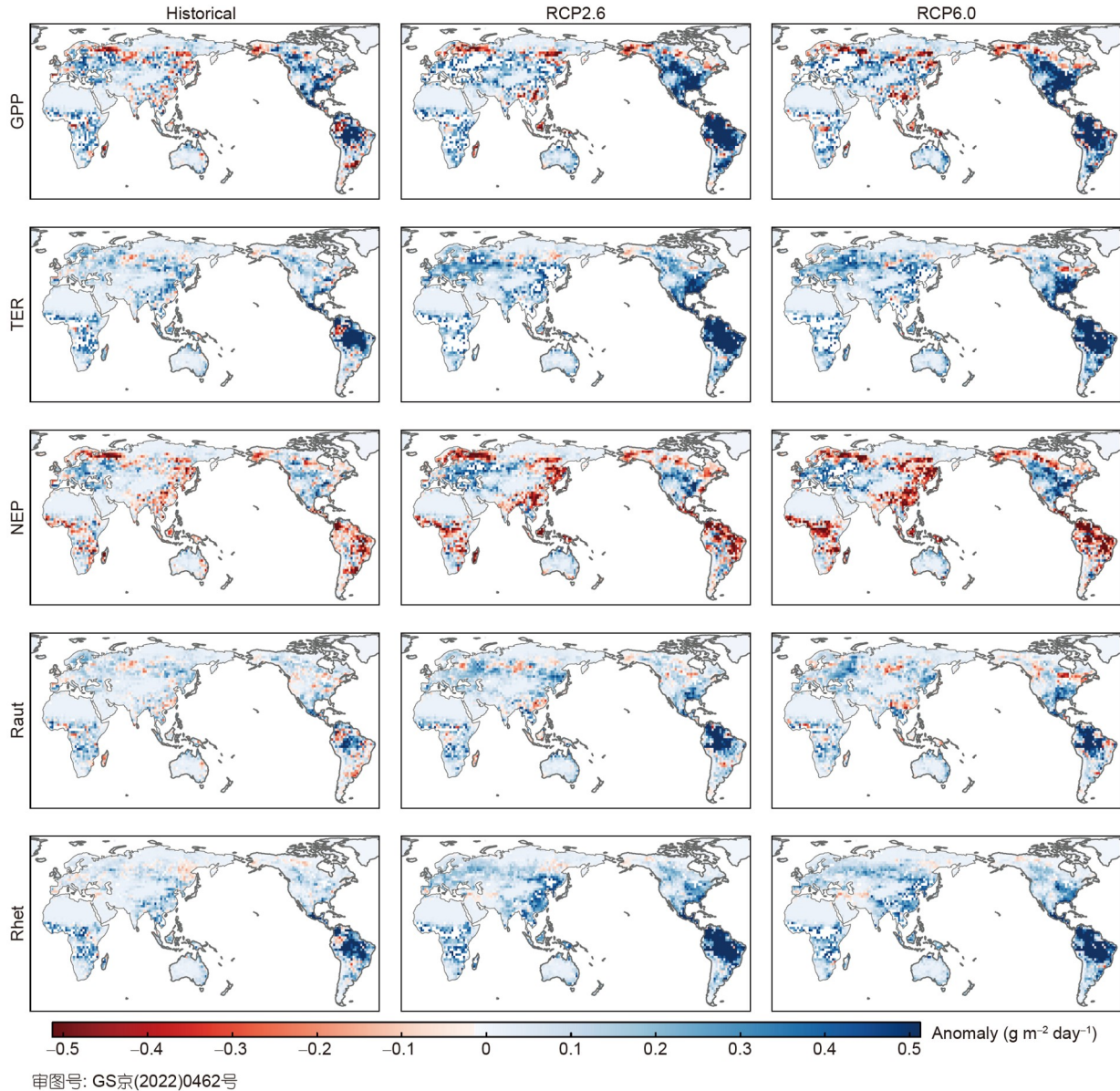
Figure 11   Anomalies in carbon variables under high precipitation extremes (higher than 90% percentile) during historical and future periods.

tremes generally show sub C-C scaling, while tropical lands (oceans) show a negative (super C-C scaling such as over 20% °C⁻¹) scaling rate. The scaling types and rates are similar under multitemporal precipitation extremes, while the different methods for defining extremes have significant impacts on the response patterns. CAPE shows a scaling rate of over 6.8% °C⁻¹, while TCWV and RH have a sub C-C scaling or a negative rate, respectively, suggesting that the declines in precipitation extremes in hotter environments as well as the hook structures can be attributed to atmospheric dynamics. In the context of global warming, the T_{pp} of the hook structure is projected to increase 1–5°C, and the scaling curves are shifting toward a warmer environment, which is projected to result in a 10–40% intensification in precipita-

tion extremes by the end of this century. Moderate levels of precipitation contribute to ecosystem carbon assimilation, and the response of the carbon budget to precipitation under climate change is stable.

This study only explores the trends in three-dimensional precipitation events; it is necessary to further examine their response patterns to atmospheric thermodynamics and dynamics and to evaluate the feedback mechanisms of the soil-vegetation-atmosphere-ocean Earth systems. The underlying physical mechanism for the formation of the hook structures is very complex. In this study, only the impacts of RH, CAPE and TCVW on precipitation are explored. The increases in convective precipitation under high temperatures, the changes in cloud microphysical structure, the decreases in wet

event duration, the cooling effects of precipitation and seasonal changes in temperature are also important for shaping the hook structures (Sullivan et al., 2020; Gao et al., 2020); therefore, these mechanisms should be further quantified. Ocean and land areas generally show different characteristics for extreme precipitation evolution, and their thermodynamic/dynamic response mechanisms may be different. It is necessary to further explore the microphysical mechanisms for the evolution of extreme precipitation events over ocean and land areas. Climate change, rapid urbanization, the construction of water conservancy projects and other influencing human activities affect extreme weather and climate events. This study mainly considers the impact of climate change, and future studies should be conducted to explore the impact of human activities on extreme precipitation and biogeochemical cycles.

References

Allan R P, Soden B J. 2008. Atmospheric warming and the amplification of precipitation extremes. Science, 321: 1481–1484

Barbero R, Westra S, Lenderink G, Fowler H J. 2018. Temperature-extreme precipitation scaling: A two-way causality? Int J Climatol, 38: e1274–e1279

Beck H E, Wood E F, Pan M, Fisher C K, Miralles D G, van Dijk A I J M, McVicar T R, Adler R F. 2019. MSWEP V2 global 3-hourly 0.1° precipitation: Methodology and quantitative assessment. Bull Am Meteorol Soc, 100: 473–500

Blöschl G, Kiss A, Viglione A, Barriendos M, Böhm O, Brázdil R, Coeur D, Demarée G, Llasat M C, Macdonald N, Retsö D, Roald L, Schmocker-Fackel P, Amorim I, Bělínová M, Benito G, Bertolin C, Camuffo D, Cornel D, Doktor R, Elleder L, Enzi S, Garcia J C, Glaser R, Hall J, Haslinger K, Hofstätter M, Komma J, Limanówka D, Lun D, Panin A, Parajka J, Petrić H, Rodrigo F S, Rohr C, Schönbein J, Schulte L, Silva L P, Toonen W H J, Valent P, Waser J, Wetter O. 2020. Current European flood-rich period exceptional compared with past 500 years. Nature, 583: 560–566

Deng S, Liu S, Mo X, Peng G. 2022. Relationship between polar motion and key hydrological elements at multiple scales. Sci China Earth Sci, 65: 882–898

Dwyer J G, O'Gorman P A. 2017. Changing duration and spatial extent of midlatitude precipitation extremes across different climates. Geophys Res Lett, 44: 5863–5871

Fowler H J, Lenderink G, Prein A F, Westra S, Allan R P, Ban N, Barbero R, Berg P, Blenkinsop S, Do H X, Guerreiro S, Haerter J O, Kendon E J, Lewis E, Schaer C, Sharma A, Villarini G, Wasko C, Zhang X. 2021. Anthropogenic intensification of short-duration rainfall extremes. Nat Rev Earth Environ, 2: 107–122

Gao X, Guo M, Yang Z, Zhu Q, Xu Z, Gao K. 2020. Temperature dependence of extreme precipitation over mainland China. J Hydrol, 583: 124595

Gao X, Zhu Q, Yang Z, Liu J, Wang H, Shao W, Huang G. 2018. Temperature dependence of hourly, daily, and event-based precipitation extremes over China. Sci Rep, 8: 17564

Good P, Chadwick R, Holloway C E, Kennedy J, Lowe J A, Roehrig R, Rushley S S. 2021. High sensitivity of tropical precipitation to local sea

surface temperature. Nature, 589: 408–414

Green J K, Berry J, Ciais P, Zhang Y, Gentine P. 2020. Amazon rainforest photosynthesis increases in response to atmospheric dryness. Sci Adv, 6: eabb7232

Jian Y, Fu J, Zhou F. 2021. A review of studies on the impacts of extreme precipitation on rice yields (in Chinese). Prog Geography, 40: 1746–1760

Koutsoyiannis D. 2012. Clausius-Clapeyron equation and saturation vapour pressure: Simple theory reconciled with practice. Eur J Phys, 33: 295–305

Lange S. 2019. Trend-preserving bias adjustment and statistical downscaling with ISIMIP3BASD (v1.0). Geosci Model Dev, 12: 3055–3070

Lenderink G, Van Meijgaard E. 2008. Increase in hourly precipitation extremes beyond expectations from temperature changes. Nat Geosci, 1: 511–514

Loeb N G, Kato S, Loukachine K, Manalo-Smith N. 2005. Angular distribution models for top-of-atmosphere radiative flux estimation from the clouds and the earth's radiant energy system instrument on the terra satellite. Part I: Methodology. J Atmos Ocean Tech, 22: 338–351

Nogueira M. 2020. Inter-comparison of ERA-5, ERA-interim and GPCP rainfall over the last 40 years: Process-based analysis of systematic and random differences. J Hydrol, 583: 124632

Piao S, Yue C, Ding J, Guo Z. 2022. Perspectives on the role of terrestrial ecosystems in the 'carbon neutrality' strategy. Sci China Earth Sci, 65: 1178–1186

Prein A F, Rasmussen R M, Ikeda K, Liu C, Clark M P, Holland G J. 2017. The future intensification of hourly precipitation extremes. Nat Clim Change, 7: 48–52

Roderick T P, Wasko C, Sharma A. 2019. Atmospheric moisture measurements explain increases in tropical rainfall extremes. Geophys Res Lett, 46: 1375–1382

Roxy M K, Ghosh S, Pathak A, Athulya R, Mujumdar M, Murtugudde R, Terray P, Rajeevan M. 2017. A threefold rise in widespread extreme rain events over central India. Nat Commun, 8: 708

Save H, Bettadpur S, Tapley B D. 2016. High-resolution CSR GRACE RL05 mascons. J Geophys Res-Solid Earth, 121: 7547–7569

Schär C, Ban N, Fischer E M, Rajczak J, Schmidli J, Frei C, Giorgi F, Karl T R, Kendon E J, Tank A M G K, O'Gorman P A, Sillmann J, Zhang X, Zwiers F W. 2016. Percentile indices for assessing changes in heavy precipitation events. Clim Change, 137: 201–216

Simmons A J, Untch A, Jakob C, Kållberg P, Undén P. 1999. Stratospheric water vapour and tropical tropopause temperatures in Ecmwf analyses and multi-year simulations. Q J R Meteorol Soc, 125: 353–386

Smith A, Lott N, Vose R. 2011. The integrated surface database: Recent developments and partnerships. Bull Am Meteorol Soc, 92: 704–708

Sullivan S C, Schiro K A, Yin J, Gentine P. 2020. Changes in tropical precipitation intensity with El Niño warming. Geophys Res Lett, 47: e2020GL087663

Sun Q, Xie Z H, Tian X J. 2015. GRACE terrestrial water storage data assimilation based on the ensemble four-dimensional variational method PODEn4DVar: Method and validation. Sci China Earth Sci, 58: 371–384

Utsumi N, Seto S, Kanae S, Maeda E E, Oki T. 2011. Does higher surface temperature intensify extreme precipitation? Geophys Res Lett, 38: L16708

Vogel E, Donat M G, Alexander L V, Meinshausen M, Ray D K, Karoly D, Meinshausen N, Frieler K. 2019. The effects of climate extremes on global agricultural yields. Environ Res Lett, 14: 054010

Wang G, Wang D, Trenberth K E, Erfanian A, Yu M, Bosilovich M G, Parr D T. 2017. The peak structure and future changes of the relationships between extreme precipitation and temperature. Nat Clim Change, 7: 268–274

Wang R, Gentine P, Yin J, Chen L, Chen J, Li L. 2021. Long-term relative decline in evapotranspiration with increasing runoff on fractional land surfaces. Hydrol Earth Syst Sci, 25: 3805–3818

Wasko C, Sharma A, Lettenmaier D P. 2019. Increases in temperature do not translate to increased flooding. Nat Commun, 10: 5676

Wen Y, Fang X, Liu Y, Li Y. 2019. Rising grain prices in response to phased climatic change during 1736–1850 in the North China Plain. Sci China Earth Sci, 62: 1832–1844

Wing O E J, Lehman W, Bates P D, Sampson C C, Quinn N, Smith A M, Neal J C, Porter J R, Kousky C. 2022. Inequitable patterns of US flood risk in the Anthropocene. Nat Clim Chang, 12: 156–162

Xu X, Xu K, Yang D, et al. 2019. Drought identification and drought frequency analysis based on multiple variables (in Chinese). Adv Water Sci, 30: 373–381

Yin J, Gentine P, Zhou S, Sullivan S C, Wang R, Zhang Y, Guo S. 2018. Large increase in global storm runoff extremes driven by climate and anthropogenic changes. Nat Commun, 9: 4389

Yin J, Guo S, Gentine P, Sullivan S C, Gu L, He S, Chen J, Liu P. 2021a. Does the hook structure constrain future flood intensification under anthropogenic climate warming? Water Res, 57: e28491

Yin J B, Guo S L, Gu L, Yang G, Wang J, Yang Y. 2021b. Thermodynamic response of precipitation extremes to climate change and its impacts on floods over China (in Chinese). Chin Sci Bull, 66: 4315–4325

Yin J, Guo S, Yang Y, Chen J, Gu L, Wang J, He S, Wu B, Xiong J. 2022. Projection of droughts and their socioeconomic exposures based on terrestrial water storage anomaly over China. Sci China Earth Sci, 65: 1772–1787

Zampieri M, Ceglar A, Dentener F, Toreti A. 2017. Wheat yield loss attributable to heat waves, drought and water excess at the global, national and subnational scales. Environ Res Lett, 12: 064008

Zeder J, Fischer E M. 2020. Observed extreme precipitation trends and scaling in central Europe. Weather Clim Extremes, 29: 100266

Zhang Y, Joiner J, Hamed Alemohammad S, Zhou S, Gentine P. 2018. A global spatially contiguous solar-induced fluorescence (CSIF) dataset using neural networks. Biogeosciences, 15: 5779–5800

Zhang Y, Commane R, Zhou S, Williams A P, Gentine P. 2020. Light limitation regulates the response of autumn terrestrial carbon uptake to warming. Nat Clim Chang, 10: 739–743

Zhou S, Zhang Y, Park Williams A, Gentine P. 2019. Projected increases in intensity, frequency, and terrestrial carbon costs of compound drought and aridity events. Sci Adv, 5: eaau5740

(Responsible editor: Qiuhong TANG)